




Article

Design of a Lightweight Origami Composite Crash Box: Experimental and Numerical Study on the Absorbed Energy in Frontal Impacts

Alberto Ciampaglia * , Luca Patruno  and Raffaele Ciardiello * 

Dipartimento di Ingegneria Meccanica e Aerospaziale, Politecnico di Torino, 10121 Turin, Italy

* Correspondence: alberto.ciampaglia@polito.it (A.C.); raffaele.ciardiello@polito.it (R.C.)

Abstract: Origami-shaped composite structures are currently being explored for their ability to absorb energy in a progressive and controlled manner. In vehicle passive safety applications, this prevents the occurrence of peak forces that could potentially cause injuries to vehicle passengers. The work presents the design of a carbon fiber-reinforced polymer (CFRP) crash box for a Formula Student race car, using a numerical model validated by experimental tests. An initial characterization of the material is conducted according to the standards. Following, six origami samples are manufactured and subjected to crash tests to gather accurate experimental data. The numerical model is validated on the tests and used for the design of the race car's impact attenuator. The designed crash box meets the Formula Student requirements while reducing the total mass by 14% and the maximum deceleration of 21% compared with the previous design. The study confirms the potential use of origami structures to improve crashworthiness while reducing vehicle weight.

Keywords: crash boxes; composite; lightweight; Formula Student



Citation: Ciampaglia, A.; Patruno, L.; Ciardiello, R. Design of a Lightweight Origami Composite Crash Box: Experimental and Numerical Study on the Absorbed Energy in Frontal Impacts. *J. Compos. Sci.* **2024**, *8*, 224. <https://doi.org/10.3390/jcs8060224>

Academic Editors: Francesco Tornabene and Thanasis Triantafyllou

Received: 19 April 2024

Revised: 23 May 2024

Accepted: 12 June 2024

Published: 14 June 2024



Copyright: © 2024 by the authors. Licensee MDPI, Basel, Switzerland. This article is an open access article distributed under the terms and conditions of the Creative Commons Attribution (CC BY) license (<https://creativecommons.org/licenses/by/4.0/>).

1. Introduction

The article presents the design of an origami-inspired crash absorber made of a carbon fiber-reinforced composite for a race car. The work focuses on the experimental characterization of manufactured prototypes, followed by the validation of the numerical models to be used in the design of the impact absorber. These origami crash absorbers are used in the Formula Student competition, which is organized by the Institution of Mechanical Engineers (IMEchE) and uses the same rules as the original Formula SAE. In this section, a general overview on the thin-walled structures for energy absorption is given. Following, the state of the art on the use of composite materials for crash structures is discussed, finally delving into the application of origami-inspired design in this field.

1.1. Crash Structures for Vehicle Safety

Crash absorber devices are components specifically engineered to absorb kinetic energy during vehicle impact events. Their primary function is to reduce the load transmitted to the passenger compartment by dissipating energy through controlled deformation and fracture mechanisms. Limiting the load peaks that occur during the impact events is crucial. Excessive load peaks can lead to high deceleration for the occupants of the vehicles, which is a high risk for passenger injuries. Specifically, crash boxes play a crucial role in preserving the structural integrity of the front car body during low-velocity impacts. These sacrificial components are designed to absorb kinetic energy during the initial stage of a frontal crash without damaging the front sub frame. The energy-absorbing response and collapsing mode of the crash boxes are highly influenced by their shape and material. Thin-walled structures, such as beams and tubes, are the most common geometries and have been intensively investigated. Abramowicz et al. [1,2] studied the axial crushing behavior of thin-walled square steel tubes with different cross-sections and formulated a

folding element theory for predicting the mean crushing force of axially crushed square box columns. Reid and Reddy [3] extended this study to single and double-tapered thin-walled tubes with rectangular sections, demonstrating the extended capability of this geometry to absorb energy in oblique impacts. Mamalis et al. [4] investigated the crushing response of circular section and *frusta* (truncated cone) tubes under axial impact, showing how these geometries could enhance the energy-absorbing capability while lowering the initial force peak.

1.2. Composite Materials for Crash Structures

In recent years, there has been extensive research on the analysis of composite materials for crush-absorbing purposes. The use of composite materials offers, together with the possibility to customize the mechanical properties with different fibers, matrices, and geometries, the opportunity to be lightweight [5–7]. The influence of fiber and matrix type, fiber orientation, tube geometry, cooling rate in the cure cycle, and fiber volume fraction on the energy-absorbing response of fiber-reinforced polymers has been extensively investigated as reviewed by Jacob et al [8], Isaac [9] and Wang [10]. The use of thermosetting carbon fiber-reinforced polymers (CFRPs) for energy attenuation purposes has been the subject of numerous studies. The intrinsic brittle failure mode of thermosetting CFRPs, coupled with debris formation during crushing, can lead to pronounced load oscillations. Consequently, optimizing the geometry and thickness of crash absorbers becomes crucial for achieving an optimal crush response. Boria et al. [11] experimentally crushed truncated conical structures made of thermosetting composite material, assessing the influence of geometrical parameters (wall thickness, cone angle, and minor internal diameter) on energy absorption capacity. Obradovic et al. [12] designed and experimentally crushed an impact attenuator for a Formula SAE vehicle made of a thermosetting composite material. Later, Boria et al. [13] tested and compared the crush response of attenuators with the same shape made of a thermoplastic composite material by finding that to avoid unstable behavior the diameter of the tubes should be carefully designed. Despite the desirable plastic crushing behavior exhibited by the thermoplastic attenuator, research outcomes underscored its limited energy absorption capacity compared to the CFRP impact attenuator.

The increasing interests towards the use of composites in crash structures raised the need for a numerical model that could accurately, yet rapidly, predict the crash response of composite parts. A modeling strategy embedding shell layers stacked with cohesive elements was first introduced in [14], where it is demonstrated to be capable of predicting the initiation and propagation of composite failure with an accuracy close to that of a solid elements model. In crash applications, cohesive elements were combined with solid [11,15] or shell [16] elements to model the response of large structures. The model presented in [15] combines cohesive with state-of-the-art techniques (e.g., fiber-oriented mesh, non-linear shear response, and tie-break controlled intra-laminar failure) to model the crash of a ± 45 tube with remarkable accuracy but requires 94 h to reach 4 ms. Ref. [17] investigated the implementation of combined shell and cohesive elements to reduce the computational cost, and reported accurate results for the out-of-plane impact of a composite plate with high computational efficiency. Ref. [16] adopted this strategy for modeling the crash of an IA, demonstrating its accuracy in the prediction of combined fragmentation and delamination of the structure. In this paper, shell and solid cohesive elements are combined to model the out-of-plane strength of the laminate. The single-shell model only allows for the tearing of the laminate, whereas the delamination is inhibited since an out-of-plane toughness is not defined.

1.3. Composite Crash Structures with Origami-Inspired Design

In the last 10 years, the adoption of crash boxes manufactured with pre-folded origami patterns for thin-walled structures has been investigated to reduce peak load and control the collapsing behavior of the tube to maximize energy absorption. The control of the collapsing behavior of crash boxes to maximize the energy absorption while reducing the

peak loads is crucial in the design of crash boxes. Indeed, these two factors reduce the deceleration experienced by the occupants during crash events, avoiding fatalities and major injuries. New origami crash boxes with squared, rectangular, polygonal cross sections, and tapered shapes, created by pre-folding the surface of thin-walled tubes, that lead to an improved collapsing behavior were studied. Ma and You [18] numerically studied the axial crushing response of origami crash boxes and demonstrated their capability to reduce peak forces while maintaining the same energy absorption level. Zhao et al. [19] proposed the geometrical optimization of steel cylindrical origami tubes to enhance the energy-absorbing capability, and similar research was conducted on different origami pattern pre-folded tubes [20–22], demonstrating the benefits of these geometries in axial crush. In recent years, crash boxes with origami shapes have been extensively studied. The response of CFRP tubes with the full-diamond pattern and its variation with curved lobes is discussed in [23]. The authors reported a significant influence of the number of faces and the twisting angle on the failure modes, ultimately governing the crashworthiness of the tubes. Ciampaglia et al. [5] conducted experimental and numerical studies on the response of CFRP origami tubes with a trapezoidal pattern. The results underline the importance of optimizing the pattern to improve crash worthiness, and the authors proposed a physics-based data-driven method to accelerate the optimization procedure [24]. Song et al. [25] proposed a hybrid CFRP/steel approach to improve the stability of the crashing response and induce diamond failure. O’Neil et al. [26] manufactured and tested pre-folded carbon fiber-reinforced plastic (CFRP) tubes featuring the Kresling fold pattern, reporting lower specific energy absorption (SEA) but superior stability of the crash force compared to squared and cylindrical tubes. Despite extensive research efforts, there is not yet a generally adopted structure with a high capability to absorb energy and limit deceleration under threshold limits. However, the literature on origami structures [5,18–23,27] shows that a customized shape can be designed to obtain a specific impact behavior. The present work aims to design and evaluate the mechanical behavior of lightweight origami CFRP crash boxes with high energy absorption capacity and limited force peaks to meet the Formula SAE requirements.

The work provides a numerical and experimental analysis of a full-scale prototype, designed to fit within the regulatory framework as described in Section 3. Six crash boxes made of CFRP were produced and tested on a drop tower with an impact velocity of 6.5 m/s. The results of the crash test, alongside the material parameters experimentally defined with tension and compression tests, were used to validate the numerical model presented in Section 4. Finally, a Finite Element Analysis (FEA) was carried out to validate a numerical model on the real impact test and then to simulate the final component that will be used on the vehicle. For the numerical modeling activity, two different approaches were used: shell and cohesive models.

2. Materials and Methods

2.1. Geometry

Origami structures are created by folding a flat sheet into a three-dimensional shape. Figure 1 illustrates one of the three basic modules that are axially stacked to create the whole crash box.

The rectangular sheet shown in Figure 1a in the unfolded configuration has a longer edge of $8e$ and a height of l , parameters which are already discussed in [5]. When the sheet is folded, an angle θ is created between the plane orthogonal to the tube axis and the folded faces. The crash box will have a sequence of square and octagonal cross-sections, with the latter one described by a width parameter c . The sheet must be rectangular when unfolded; therefore, it follows that

$$8b + 4c = 8e. \quad (1)$$

This implies that the height of the module h is smaller than the height l of the sheet. According to the Formula SAE rules, the crash box must have dimensions $210 \times 100 \times 100$ mm. The design space can accommodate two origami crash tubes with the base dimensions of

the single module reported in Table 1. Although the variations of b and c do not change the total mass of the crash box, they affect the crash response and should be optimized accordingly [5].

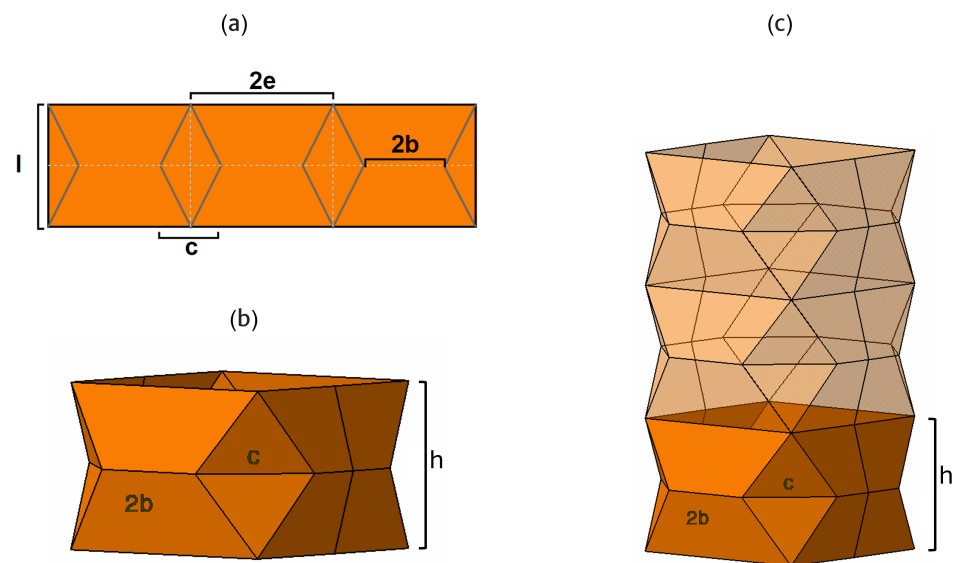


Figure 1. Structures description: (a) single module unfolded configuration, (b) single module folded configuration, (c) whole crash-box.

Table 1. Description of single module parameters.

	Parameter	Dimension
Single module	θ	1.28 rad
	b	25 mm
	c	50 mm
	h	70 mm
	l	73 mm

2.2. Materials

The composite crash boxes were produced by using epoxy carbon-based prepreg, Tenax HTA-DT806W42 from DeltaPreg (Teramo, Italy). This prepreg is constituted of twills, and Tenax HTA-3k carbon fibers, from Toray (Tokyo, Japan). This is a 2×2 woven fabric that presents an areal weight of 200 gsm and a twill wave of 3 k. Composite laminates were fabricated to produce tensile and compressive specimens that were used as input data for material card parameters. Thirteen layers of prepreg were used to fabricate the composite laminates. Two molds were used on the bottom and top of the laminates and then were vacuumed before the curing in the autoclave. The laminates were cured under a pressure of 5 bar and a temperature of 65 °C for 30 min followed by a temperature of 120 °C for 120 min.

Experimental Characterization

The tensile tests were executed using an Instron 8801 testing machine (Instron, Norwood, MA, USA) equipped with a 100 kN load cell. As reported in ASTM D3039 Standard [28], the testing cross head speed was set to 2 mm/min. The strain values in both the longitudinal and transversal orientations were measured by strain gauges, HBM 1-LY48-3/350) purchased at HBM (Hørning, Denmark), and positioned in the center of the specimens. This allowed us to determine the Young’s modulus. As outlined in ASTM D3039, the specimens present a rectangular cross-section, a width of 25 mm, a thickness of 2.9 mm, and a length of 250 mm. For precise stress calculations during the tests, the actual width and thickness of each specimen were measured using a digital caliper with a resolu-

tion of 0.01 mm. National Instruments NI 9237 were used to properly acquire the signal. Four specimens were tested.

Compression tests were carried out using the ASTM Standard D3410 [29]. Specimens with rectangular cross-sections and nominal width equal to 13 mm, a thickness of 2.9 mm, and a length of 150 mm were tested. An anti-buckling fixture, as reported in the ASTM D3410, was used to avoid the bending of the specimen. The unclamped length of 10 mm was set during the tests. A cross head speed of 1.3 mm/min was used for these tests. The strain was measured with a strain gauge (HBM 1-LY48-3/350) attached at the center of the unclamped length, and the National Instruments NI 9237 system was employed for properly acquiring the strain signal. Four specimens were tested.

These are the parameters that were used in the model that was used in FEM simulations (Table 2). On the other hand, the shear properties were provided by the material supplier. The shear modulus was set to 3.5 GPa and the shear strength 120 MPa.

Table 2. Mechanical properties of the CFRP: elastic modulus in tensile (E_T) and compression (E_C), ultimate tensile strength (UTS), and ultimate compression strength (UCS).

	UTS [MPa]	E_T [GPa]	UCS [MPa]	E_C [GPa]
Mean Value	705	57.9	611	57.9
DEV.STD	36.19	0.25	37.42	0.15

2.3. Tube Manufacturing

The crash tubes used in the impact tests were produced with the hand layup of the prepregs following an autoclave curing of the preformed part. Aluminum and epoxy resin molds were used to laminate the origami tubes as shown in Figure 2a. Both molds were manufactured with a clearance angle of 3° to accommodate the de-molding of the part. To achieve a gradual crashing, the thickness of the single modules is increased from the crash front to the base of the crash box. The thickness variation is complied by varying the number of laminae in each module, with the external ply being common to all the modules and the inner plies trimmed to achieve such variation. As a result, the first module had 3 layers; the second had 6 layers; and the third had 9 layers. The adoption of modules with increasing thickness promotes a progressive failure of the crash box as found in a preliminary study. The final thickness after curing measured 0.69 mm, 1.38 mm and 2.07 mm, respectively, for the three modules. While the geometry of the origami tube was defined to accomplish the SAE regulation, the thickness of the tube was estimated on the base of a previous study [5].

Figure 2 shows the different phases of the manufacturing process: first, the prepreg is layered within half molds according to the defined stacking sequence; the two halves of the mold are then placed together, either by overlapping Figure 2(b.1) or not Figure 2(b.1) the plies; and the part undergoes pre-curing to consolidate the layers and is finally cured in the autoclave to obtain the final part. To join the two halves of the specimen, a *strip* method and *overlap* criteria were approached. For the strip method, crash box parts are laminated separately and when one mold is positioned on top of the other, three strips (20 mm of width) are added Figure 2(c.1). With the overlap method, the plies are positioned in a complementary way in the two molds, shifting them 5 mm each, yielding an offset of the joining lines as shown in Figure 2(c.2). The overlap techniques allow shifting the joining lines of the two adjacent parts, which represent a weak area of the part. This configuration conceives a redistribution of the stresses and avoids the interaction of the stress intensification induced by the material discontinuity.

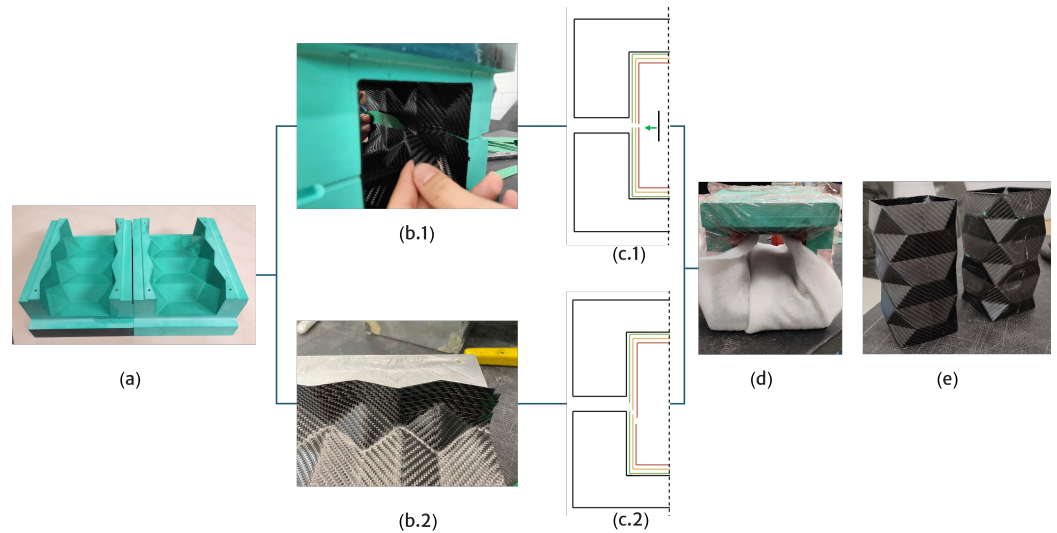


Figure 2. Manufacturing process: (a) Epoxy resin mold. (b.1) Strip lamination criteria. (b.2) Overlap lamination criteria. (c.1) Detailed strip frontal view. (c.2) Detailed overlap frontal view. (d) Breather. (e) Final product. The arrows indicate the manufacturing sequence.

3. Numerical Modeling of the Axial Crash of the Origami Crash Box

The numerical model was developed using LsDyna R13.1.0 (Ansys Inc., Livermore, CA, USA). Given the prismatic symmetry of the origami-shaped tubes, only a quarter of the structure was modeled and symmetric boundary conditions were applied. The intra-laminar damage behavior of the woven plies was modeled with the Continuous Damage Model, while Continuous Zone Modeling was used to describe the inter-laminar delamination.

The elements that were fully damaged were deleted during the simulation to replicate the crack formation and propagation during the crash and avoid convergence issues caused by highly distorted elements. A moving rigid wall with a mass of 480 kg, the same as the hammer used in the experimental test, and an initial speed of 3.615 m/s was implemented to simulate a kinetic energy of 3200 J. The contact between the wall and the part was modeled using the AUTOMATIC_SINGLE_CONTACT with a dynamic friction coefficient of 0.2, typical for CFRP–steel contact. The mesh size was set to 3 mm after a convergence study. The integration time step was set to 5 ms and hourglass energy control using Flanagan–Belytschko criteria was implemented. The simulation time was set to 80 ms.

Two different modeling approaches were investigated: (a) *shell* model with one shell element through the thickness, and (b) a *hybrid* model with multiple shell elements stacked with cohesive elements. The model setup is illustrated in Figure 3.

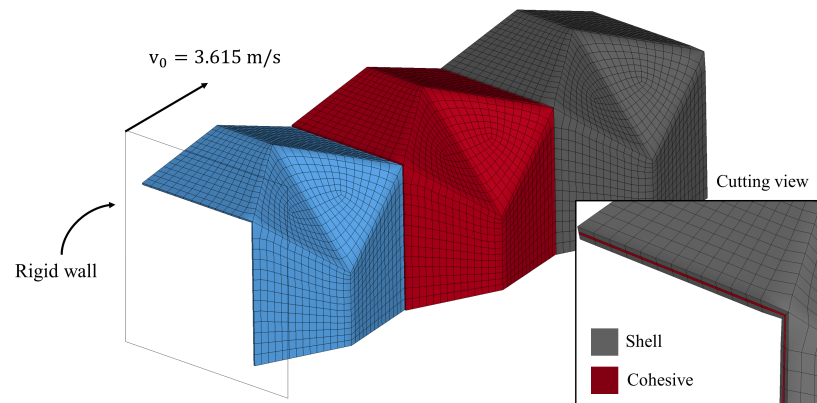


Figure 3. Numerical model of the crash test and detailed view of cohesive modeling.

3.1. Shell Model

The laminates are modeled with shell elements using the Gauss reduced integration rule with four points in the plane and one integration point for each ply through the thickness. The shell approach models the carbon fiber plies with a single layer of shell elements using a First Order Shear Deformation Theory to simulate the laminate response. The *shell* model was modeled solely by the shell element. Each post-cure ply thickness was set to 0.23 mm, yielding a total thickness of 0.69 mm, 1.38 mm, and 2.07 mm for the three modules, respectively. Fully integrated shell elements (ELFORM = 16) were used with a shear correction factor equal to 0.625.

3.2. Hybrid Model: Shell and Cohesive

The *hybrid* model contains thin modules modeled with shell elements only and thicker modules modeled with shell elements connected by solid cohesive elements. More precisely, the first module is modeled with shell elements only since the absorbed energy is assumed to be related to in-plane failures because of its reduced thickness. The thicker modules are modeled with combined shell and cohesive elements to allow for the delamination of the composite. The energy absorbed by the second and third modules is assumed to have both contributions from the intra-laminar and inter-laminar strength, given its larger thickness. As a rule of thumb, the thickness associated with the cohesive elements was set to one-fourth of the ply's total thickness. The cohesive model is summarized in Table 3 with a detailed description of each module.

Table 3. Thickness of the shell and cohesive elements used to model the CFRP laminate of each module.

	Plies	Shell Thickness [mm]	Cohesive Thickness [mm]
Module #1	3	0.69	-
Module #2	6	1.38	0.345
Module #3	9	2.07	0.5175

The cohesive layer was modeled with 8-noded solid elements (ELFORM = 20), where the traction force is computed from the displacement between nodal pairs interpolated on four integration points. The element is featured with an offset distance to work in combination with shell elements and properly apply moments computed from the nodal forces.

3.3. Constitutive Modeling

The elastic response of the woven is modeled with a linear orthotropic law. The intra-laminar damage is modeled with an orthotropic failure surface described with the Chang–Chang criterion. Given the balanced nature of twill woven composite, only compression and tension are here distinguished, while the properties along the two principal directions are assumed to be the same. The stress-based criterion defines the elastic limit of the lamina upon three failure indices e_f , e_c and e_s , respectively associated with the tensile fiber failure, compression fiber failure, and matrix failure (only associated with the shear). The failure indices e_f , e_c and e_s are defined at each ply by the tensile strength (X_T), the compression strength (X_C), and the shear strength (S_C) as:

$$e_f^2 = \left(\frac{\sigma_{ii}}{X_T}\right)^2 + \beta \left(\frac{\sigma_{ij}}{S_C}\right)^2 - 1 \quad \text{if } \sigma_{ii} \geq 0, \quad i = 1, 2 \tag{2}$$

$$e_c^2 = \left(\frac{\sigma_{ii}}{X_C}\right)^2 - 1 \quad \text{if } \sigma_{ii} < 0, \quad i = 1, 2 \tag{3}$$

$$e_m^2 = \left(\frac{\sigma_{ij}}{S_C}\right)^2 - 1, \quad i, j = 1, 2 \tag{4}$$

Whenever the failure indices reach zero, the material undergoes a strain-based progressive damaging described by the ultimate strain values d_{fail}^c , d_{fail}^t , and d_{fail}^s , respectively defining the ultimate failure for the compression, tensile, and shear mode. The element is deleted when all the integration points are failed. The model uses the *Enhanced Composite Damage* constitutive law developed by *LsDyna (AT_054-055)* which features a strength reduction in the *crash-front* elements (i.e., elements sharing nodes with a deleted element) by a factor defined with the *SOFT* parameter.

The inter-laminar behavior is modeled with a triangular traction–separation law used for the cohesive elements. The model encompasses a quadratic mixed mode delamination criterion defined with the mode I fracture toughness G_{Ic} and the ultimate stress σ_{max} in the *MAT138*.

3.4. Manufacturing Induced Variations

The formation of sharp edges during the manufacturing of laminates induces a local variation of the micro-structure that stretches or wrinkles to accommodate the geometry. These local alterations cause a reduction in the material properties, which is particularly evident when compression stresses are applied. Local alterations of the prepreg were predicted with the draping simulation tool from *Hypermesh (Altair Inc., Troy, MI, USA)*. Figure 4a reports the result of the draping simulation. Because of the sharp edges, the material in the rhomboidal diagonal is shrunk, and reduced material properties are expected in that area as shown in Figure 4b by projecting the numerical result on the manufactured crash box. The mesh elements associated with a shrinkage factor higher than 80% are identified as triggers, and their material properties are reduced to replicate the degradation and promote the failure initiation. The result of the simulations, shown in Figure 4c, displays that these are the areas where the failure starts. The reduced properties are reported in Table 4.

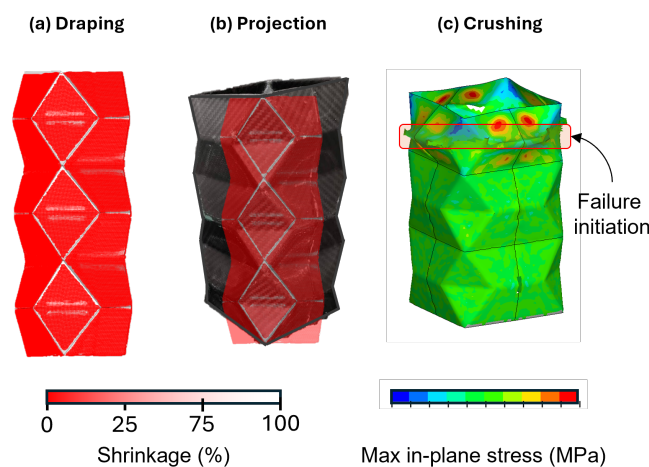


Figure 4. (a) Amount of woven shrinkage predicted with the draping simulation, (b) corresponding regions of the manufactured crash box, and (c) failure initiation promoted by the manufacturing imperfections.

Table 4. Material properties used for the trigger elements.

Property	CFRP	CFRP Trigger
$E_1 (=E_2)$	57.9 GPa	57.9 GPa
X_T	605 MPa	605 MPa
X_C	612 MPa	612 MPa
G_{12}	4.0 GPa	4.0 GPa
S_C	120 MPa	120 MPa
ν_{12}	0.0835	0.0835
$G_{23} (= G_{13})$	3.7 GPa	3.7 GPa
$\nu_{23} (= \nu_{13})$	0.083	0.083
d_{fail}^s	0.04	0.04

Table 4. Cont.

Property	CFRP	CFRP Trigger
d_{fail}^t	0.0345	0.0345
d_{fail}^c	−0.1	−0.01
SOFT	0.65	0.9

4. Experimental Crash Test and Comparison with Numerical Results

The experimental setup involves a vertical sledge with a total mass of 480 kg with the specimen attached to its base as shown in Figure 5. The main axis of the origami tube is aligned with the vertical axis, simulating the frontal impact.

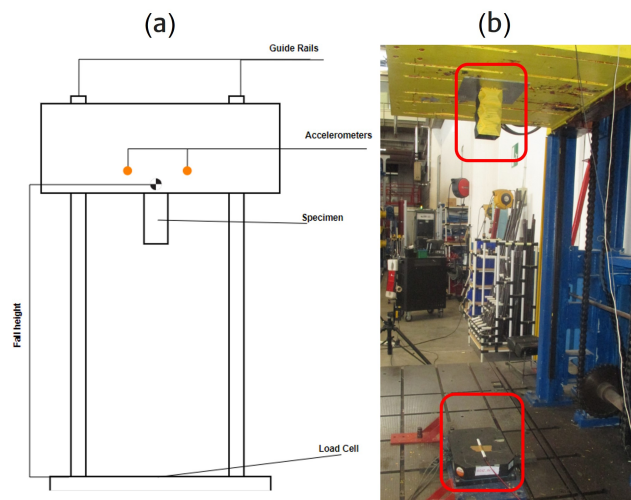


Figure 5. Sled hammer testing machine: (a) system frontal view, (b) real side view. The red boxes indicate the specimen (top) and the load cell (bottom).

In addition, the crash tests were recorded with a high-speed camera with a resolution of 1280×800 pixels and a frame rate of 1000 fps.

Data were synchronously acquired thanks to a disposable trigger placed on top of the load cell. The kinetic energy at the impact was gradually increased in the first experiments until a value of 3200 J was defined, corresponding to an initial height of the hammer equal to 0.68 m. The specimen was fastened to the base of the impacting mass with a steel plate using four screws, while the load cell was placed at the base of the test rig. The load was recorded at an acquisition frequency of 200 kHz and filtered with an analogue filter at 5 kHz (Figures 6d and 7d). Two accelerometers were placed on the sledge, on the left and right sides of the specimen. The acceleration signals were averaged to counter any rotational oscillation and processed with a low-pass filter with a cut-off frequency of 200 Hz. The experiments were repeated four times for the *strip* part and twice for the overlap one. The test conditions of the experiments are reported in Table 5.

Table 5. Experimental conditions of the crash tests.

Manufacturing	Exp #	Mass [kg]	Height [m]	Energy [J]
Strip	1	480	0.53	2496
Strip	2	480	0.55	2590
Strip	3	480	0.68	3200
Strip	4	480	0.68	3200
Overlap	1	480	0.68	3200
Overlap	2	480	0.68	3200

The average deceleration of the impact mass was integrated once to obtain the velocity reduction and twice to obtain the vertical displacement. The initial velocity was computed from the initial eight, assuming a negligible dissipation caused by air drag and contact frictions of the sliding elements. The average decelerations, the computed velocities, and the computed displacements for the strip and the overlap crash boxes are reported in Figures 6 and 7, respectively. The computed time histories were processed using a Savitzky–Golay filter with an eighth-order polynomial interpolation on a time window of 7.5 ms, corresponding to 151 samples.

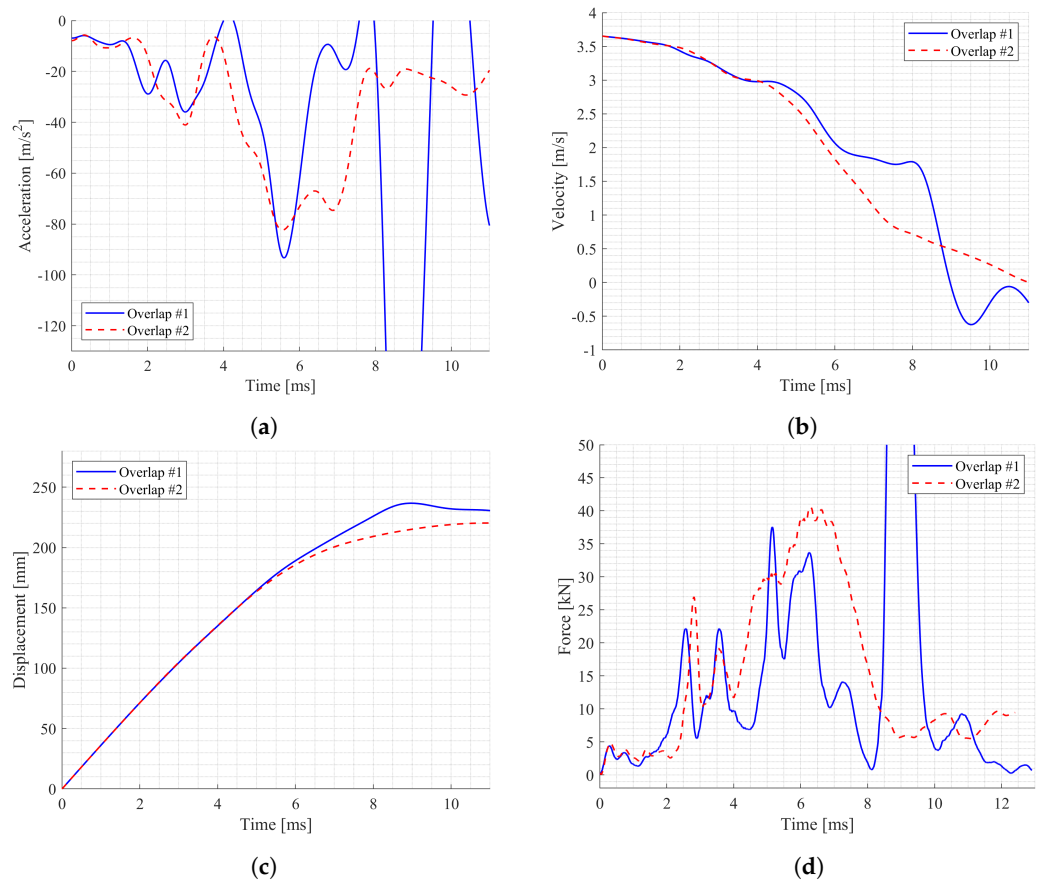


Figure 6. Results of the overlap tests: measured accelerations (a), computed velocity (b) and displacement (c) of the impact mass, and force measured from the load cell at 200 kHz (d).

Experiments *Strip #1* and *Strip #2* had a lower impact energy, causing a lower deceleration with a larger duration of the impact. Increasing the impact energy to 3200 J led to an increase in the crushing force, not sufficient to fully stop the impact mass that went in contact with the ground causing a steep increase in the load signal around 9 ms. Experiments *Overlap #1* and *Overlap #2*, performed on the overlap crash boxes, showed a different behavior: in the first, a force spike was observable after the tube crash, suggesting an incomplete absorption of the impact energy, while the latter reported an almost null velocity at the end of the impact, meaning that the kinetic energy was completely dissipated by the structure. As a result, the velocity curve shows three distinguished regions with different slopes, respectively associated with the three modules of the origami crash box. Moving further, the slope progressively reduces because of the increasing thickness of the modules, which controls the crashing force.

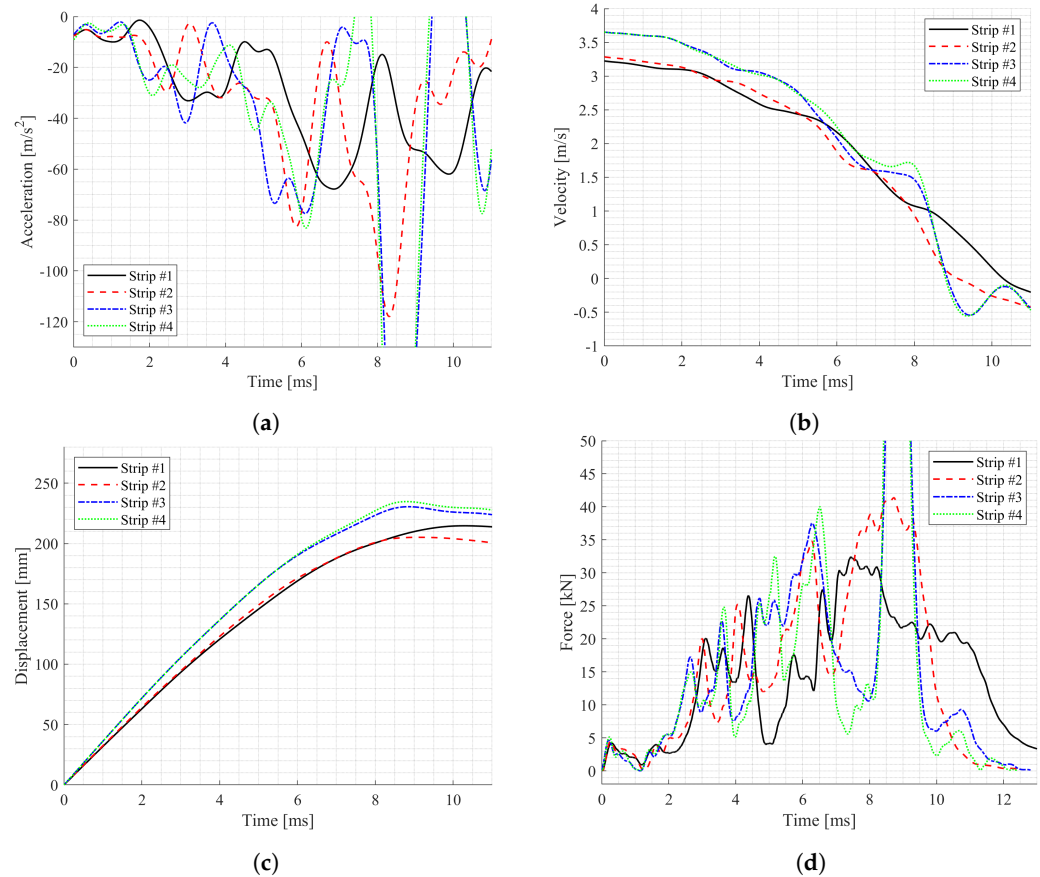


Figure 7. Results of the strip tests: measured accelerations (a), computed velocity (b) and displacement (c) of the impact mass, and force measured from the load cell at 200 kHz (d).

Absorbed Energy

The energy absorbed by the crash box is computed as the integral of the measured force over the total displacement. In Figure 8 are reported the results of the crash tests of the strip and overlap specimens. In Figure 8a–c, it can be observed that the force increases when the crash front reaches an interface region between two modules (approximately 70 mm and 140 mm), following a second peak induced by the transition from the squared to the octagonal section. In particular, the first module of the overlap specimen can absorb the kinetic energy with an almost constant force, yielding a constant deceleration of 1.05 g, while the remaining modules present an oscillating force response due to an abrupt break of the part. Together with the dissipated energy associated with friction, the absorbed energy reduces the kinetic energy of the impact mass as described in Figure 8b,d.

Overall, the overlap production method is preferable to the strip one because of its regular trend during the crash initiation and its overall superior crashworthiness. It can be concluded that the strip introduces a discontinuity in the bonding line, yielding a stress concentration that eventually worsens its energy absorption capabilities.

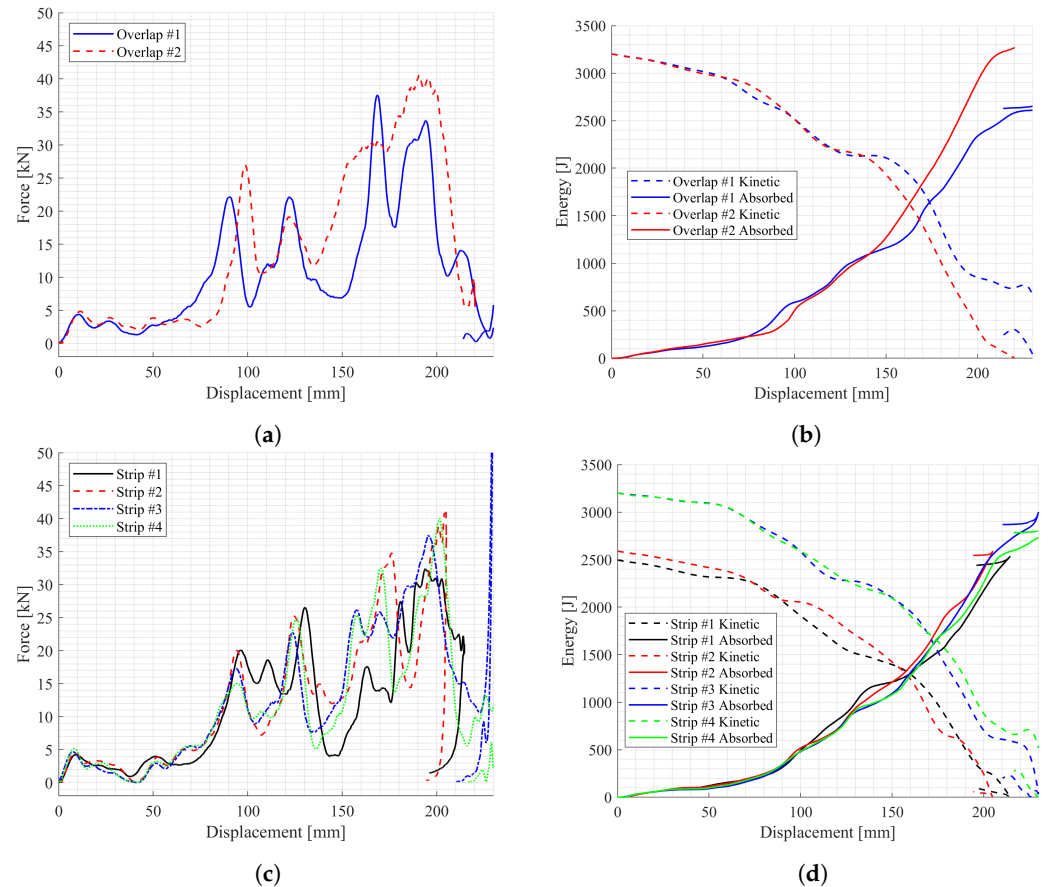


Figure 8. Force over displacement for the overlap (a) and strip (c) specimen. Kinetic energy of the impact mass and absorbed energy for the overlap (b) and strip (d) specimen.

The impact and absorbed energies of all the tests are reported in Table 6.

Table 6. Absorbed energy and production method of the specimen tested.

Manufacturing	Exp #	Impact Energy [J]	Absorbed Energy [J]
Strip	1	2496	2496
Strip	2	2590	2590
Strip	3	3200	2900
Strip	4	3200	2950
Overlap	1	3200	2750
Overlap	2	3200	3200

5. Results

In this section, the numerical results obtained with different modeling strategies, namely, the *shell* model and the *hybrid* model, are compared with the experiments to discuss their accuracy. The experimental data from both the *overlap* and the *strip* crash box are considered.

In Figure 9a,b, the force response predicted with the *shell* model is compared with the experimental curves: it can be observed that the initial force peak is accurately predicted, with an average error of 8%. The stiffness of the crash-box appears to be higher than the experimental one; however, this can be related to edge imperfections and the presence of the disposable trigger at the base of the crash bed, both promoting a gradual contact between the crash box and the ground. In the numerical model, conversely, the contact is instantaneous with a steep increase in the load up to the first failure.

The *shell* model inaccurately predicts the experimental behavior behind the crash initiation, especially after the second peak where the crash front transitions from the first module

(with 3 plies) to the second one (with 6 plies). The transition to the thicker module takes place at a displacement approximately equal to 70 mm. Figure 9c,d indicate that modeling the crash box without allowing for any separation of the laminae yields an underestimation of the absorbed energy. Indeed, only the in-plane failures can dissipate the internal energy of the material, while the delamination contribution can not be accounted for, eventually predicting an absorbed energy 53% lower than the one experimentally observed (Table 7).

The *hybrid* model overcomes the shortcoming of the *shell* model and accurately predicts the crash force response of the second module. The transition to the thicker region triggers a cohesive failure corresponding to the delamination of the composite Figure 10. This promotes a higher-energy absorption mechanism that is typically associated with the formation of two opposite fringes. As discussed in Section 4, two characteristic points can be defined for each module: a first peak force corresponding to the crash initiation and a second one corresponding to the transition from the squared to the octagonal sections. For the second module, the *hybrid* model predicts a first peak of 17.8 kN—referred to as point B in Table 7—while the average experimental value is 18.5 kN, yielding a relative error of −4.1%. The second peak—namely, point C in Table 7—is accurately predicted with an average error of −8.4%. In the third and last module, the experimental curves of the overlap tests diverge as discussed in Section 4, with one test showing a superior crashworthiness with a flat response of the crash force and a lack of the characteristic peaks previously discussed. The difference in the crash response will be the object of further investigation, while only the lower curve (*Overlap #1*) will be considered for the sake of numerical validation. For the strip tests, the experimental results of *Strip #3* are taken as reference to compute the errors. The crash initiation force of the third module values 35.0 kN, whereas the *hybrid* model predicts a lower strength with a maximum load of 31.1 kN. The last peak (point E) is accurately predicted for the overlap while being underestimated in the strip tests, yielding an average relative error of −12.3%.

It is crucial to highlight the enhanced capability of the *hybrid* model compared to the *shell* in capturing the carbon fiber delamination effect during crashes in the thick modules, where the delamination failure is predominant. At a displacement value of 70 mm and 140 mm, the transition between modules introduces the peculiar force spike, which is accurately predicted. A notable achievement of this model lies in its accurate prediction of peak force and, consequently, the maximum deceleration, with minimal error, summarized in Table 7. As a result, the absorbed energy predicted with the *hybrid* model is close to the experimental one, except for the third crash region, where the experiments diverge and the numerical model is found to be following the experimental response with lower energy.

Table 7. A comparison of the predicted peak force and absorbed energy with the experimental values from the overlap and strip tests.

	Peak Forces [kN]					Energy [J] Absorbed
	A	B	C	D	E	
Overlap #1	6.1	22.2	22.1	37.5	33.7	1949
Strip #3	5.2	14.9	24.8	32.5	40.0	1793
Average	5.6	18.5	23.4	35.0	36.5	1871
Hybrid model	6.7	17.8	21.5	31.1	32.3	1375
(Err. %)	(+18.5%)	(−4.1%)	(−8.4%)	(−11.1%)	(−12.3%)	(−26%)
Shell model	5.2	-	-	-	-	871
(Err. %)	(−8.0%)	-	-	-	-	(−53%)

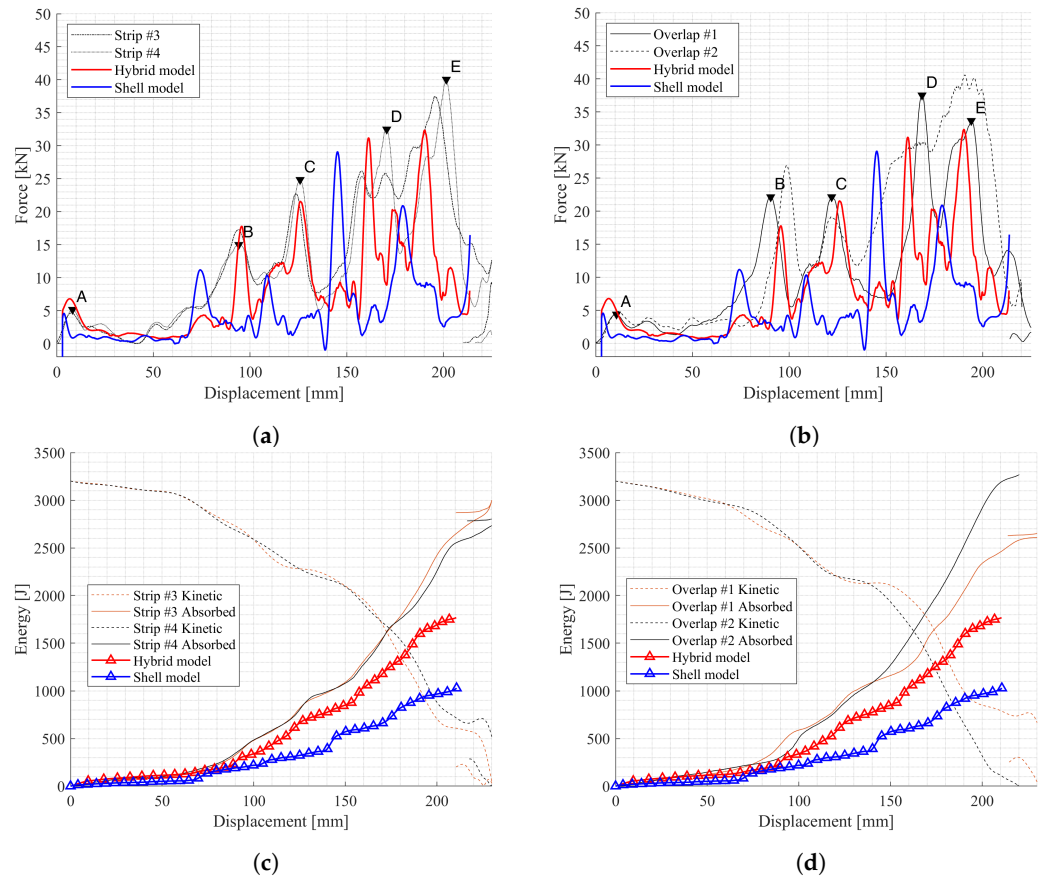


Figure 9. The crash force predicted with the hybrid and shell models compared with the experiments on the strip (a) and overlap (b) samples. The absorbed energy predicted with the numerical models compared with the strip (c) and overlap (d) tests.

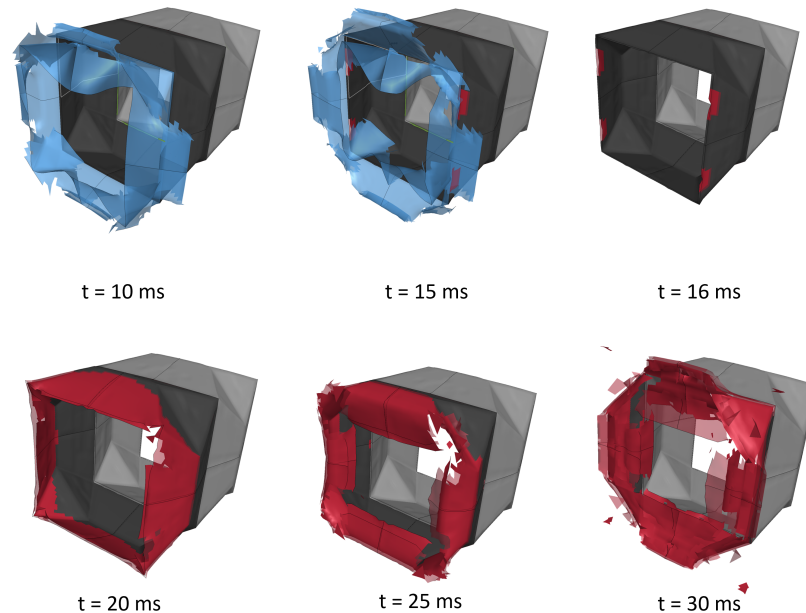


Figure 10. A three-dimensional view of the numerical model at progressive stages of the crash.

5.1. Failure Mechanism

A visual comparison between the experiments and *hybrid* model is presented in Figure 11, where the high-speed camera images of the overlap crash test (*Overlap #1*) are compared with the corresponding deformation predicted with the model. The crash

initiates with a failure of the tube folding, where the manufacturing imperfections are expected to be according to the draping simulation. The model can precisely mirror the real initiation and subsequent progression of the crash failure thanks to the modeling of these local imperfections as described in Section 3.

The material debris formed during the crash cover the camera, compromising the frames recorded after 20 ms. However, it can be appreciated that the failure progressively advances in the model, according to what was observed experimentally. Furthermore, the inward–outward alternating folding of the modules that can be observed in the images is correctly predicted by the model, suggesting the prediction of a failure mechanism coherent with the real one.

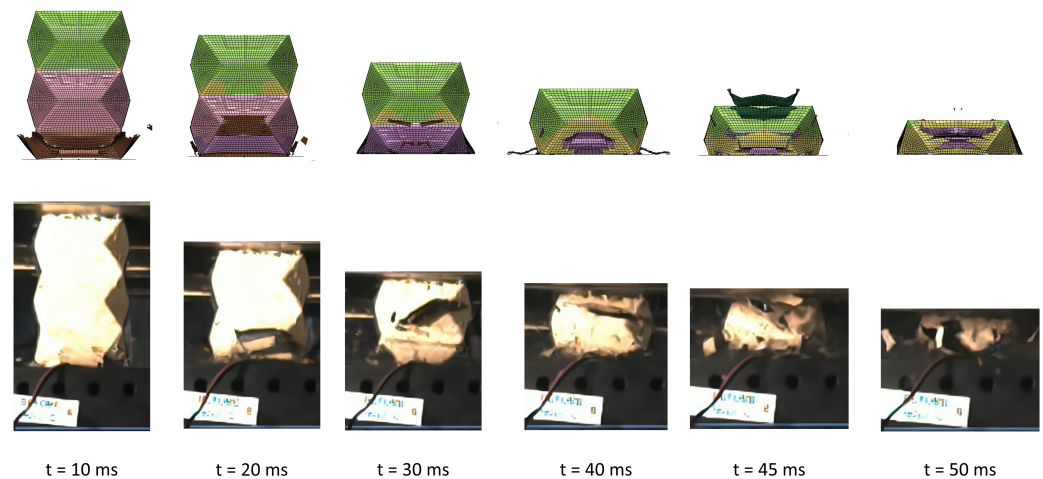


Figure 11. The failure mechanism predicted with the hybrid model (**top**) is compared with the experimental images acquired with the high-speed camera (**bottom**).

As previously discussed, the initial peak force results from a failure in the rhomboidal cross-section, while the subsequent peak is attributed to the unfolding of the origami module outside the crash box, clearly depicted in the crush frames in Figure 10. The dynamics governing the thicker modules differ significantly, where a crack propagates in the transition region, promoting an internal folding of the origami. The predominant contribution now comes from delamination failure as observable in Figure 10.

5.2. Design of the Impact Absorber

The hybrid model, incorporating both shell and cohesive elements, outperforms the shell model in simulating the crash behavior of origami-shaped composite structures. Several key factors underpin this superiority: the mixed model captures critical inter-laminar failure modes, including delamination and fiber–matrix debonding. These failure modes are essential for understanding the energy absorption mechanisms inherent in composite materials. Furthermore, it adeptly reproduces the fracture-triggering impact of origami geometry, which promotes a reduction in the peak force and a more progressively controlled crushing behavior. In terms of results accuracy, encompassing force–displacement curves, energy absorption, and specific energy absorption, the hybrid model demonstrates better performance compared to the shell model.

Finally, the numerical model is employed to determine the ultimate layup configuration in compliance with FSAE rules. Accordingly, the impact attenuator must be located forward of the front bulkhead, with a minimum width of 200 mm, and a shape compatible with other primary structures. It must be able to withstand a 300 kg mass impact at 7 m/s without exceeding a peak deceleration of 40 g or an average deceleration of 20 g, [30]. The IA structure features a parallel arrangement of two crush boxes, fixed to a honeycomb and CFRP sandwich panel. The honeycomb sandwich is modeled using the material card MAT138 from LsDyna, developed for honeycomb structures.

The interaction between the honeycomb panel and the composite parts is modeled with a node-to-surface contact formulation using a contact stiffness to prevent con-penetration and a Coulomb's friction model to model the tangential interaction. The final design encompasses a 5-7-10 plies structure, Figure 12, which guarantees a notable enhancement in performance. The designed structure boasts an energy absorption capacity of 7400 J, with an average deceleration of 7.9 g and a peak deceleration of 32 g. In direct comparison to the preceding design, characterized by three honeycomb aluminum blocks (Al 5052 5.2–1/4) each 80 mm high, the new structure excels with a higher specific energy absorption (SEA) and a lower crush force efficiency. This implies a superior capability to absorb more energy per unit mass, ensuring a more progressive and stable crushing behavior, yielding a remarkable mass reduction of 14% and a mean deceleration improvement of 21%.

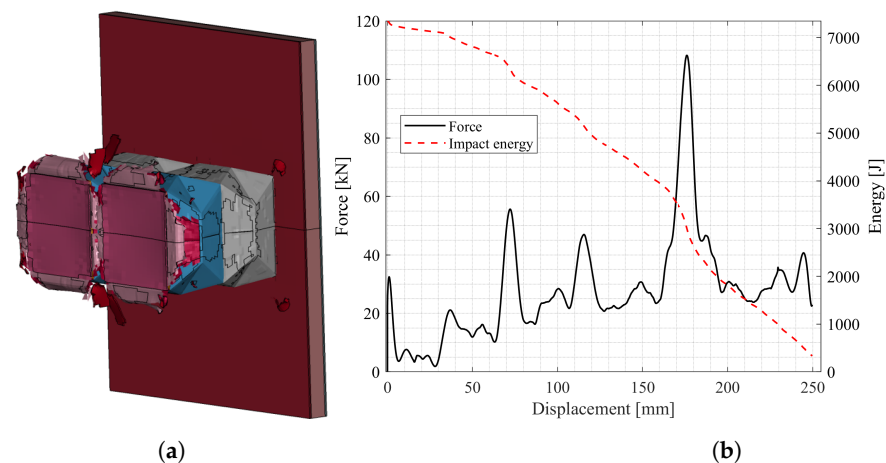


Figure 12. The model of the IA comprising the two origami crash boxes and the honeycomb panel to be fastened to the car body (a), and the results in terms of impact force and absorbed energy (b).

5.3. Conclusions

The present work reports an experimental and numerical study on the mechanical behavior of origami crash boxes under real impact conditions. The work aims to analyze two different types of structures based on manufacturing strategy: a strip of prepreg to close the origami tube and shifted overlaps. The experimental tests showed that there is not a significant difference between the absorption capabilities of the two types of structures. Further, two different modeling strategies were adopted to simulate the mechanical behavior of the crash boxes: the shell and the hybrid (cohesive and shell elements). The hybrid model, incorporating both shell and cohesive elements, outperforms the shell model in simulating the crash behavior of origami-shaped composite structures. Several key factors underpin this superiority: the mixed model captures critical inter-laminar failure modes, including delamination and fiber–matrix debonding. These failure modes are essential for understanding the energy absorption mechanisms inherent in composite materials. Furthermore, it adeptly reproduces the fracture-triggering impact of origami geometry, which promotes a reduction in the peak force and a more progressively controlled crushing behavior. In terms of results accuracy, encompassing force–displacement curves, energy absorption, and specific energy absorption, the hybrid model demonstrates better performance compared to the shell model.

Author Contributions: Conceptualization, A.C. and R.C.; methodology, A.C., L.P. and R.C.; investigation, L.P.; resources, A.C., R.C. and L.P.; writing—original draft preparation, L.P.; writing—review and editing, A.C. and R.C.; supervision, A.C. and R.C. All authors have read and agreed to the published version of the manuscript.

Funding: This research received no external funding.

Data Availability Statement: Dataset available on request from the authors.

Conflicts of Interest: The authors declare no conflicts of interest.

Abbreviations

The following abbreviations are used in this manuscript:

IA	Impact Attenuator
CFRP	Carbon Fiber-Reinforced Polymer
FSAE	Formula of Society of Automotive Engineers
SEA	Specific Energy Absorption

References

1. Abramowicz, W. The effective crushing distance in axially compressed thin-walled metal columns. *Int. J. Impact Eng.* **1983**, *1*, 309–317. [[CrossRef](#)]
2. Abramowicz, W.; Jones, N. Dynamic axial crushing of circular tubes. *Int. J. Impact Eng.* **1984**, *2*, 263–281. [[CrossRef](#)]
3. Reid, S.R.; Reddy, T.Y. Static and dynamic crushing of tapered sheet metal tubes of rectangular cross-section. *Int. J. Mech. Sci.* **1986**, *28*, 623–637. [[CrossRef](#)]
4. Mamalis, A.G.; Johnson, W. The quasi-static crumpling of thin-walled circular cylinders and frusta under axial compression. *Int. J. Mech. Sci.* **1983**, *25*, 713–732. [[CrossRef](#)]
5. Ciampaglia, A.; Fiumarella, D.; Boursier Niutta, C.; Ciardiello, R.; Belingardi, G. Impact response of an origami-shaped composite crash box: Experimental analysis and numerical optimization. *Compos. Struct.* **2021**, *256*, 113093. [[CrossRef](#)]
6. Ciampaglia, A.; Ciardiello, R.; Cesano, F.; Belingardi, G.; Brunella, V. Multifunctional material design for strain sensing: Carbon black effect on mechanical and electrical properties of polyamides. *Compos. Struct.* **2023**, *304*, 116373. [[CrossRef](#)]
7. Ciardiello, R.; Fiumarella, D.; Belingardi, G. Enhancement of the Mechanical Performance of Glass-Fibre-Reinforced Composites through the Infusion Process of a Thermoplastic Recyclable Resin. *Polymer* **2023**, *15*, 3160. [[CrossRef](#)]
8. Jacob, G.C.; Fellers, J.F.; Simunovic, S.; Starbuck, J.M. Energy Absorption in Polymer Composites for Automotive Crashworthiness. *J. Compos. Mater.* **2002**, *36*, 813–850. [[CrossRef](#)]
9. Isaac, C.W.; Ezekwem, C. A review of the crashworthiness performance of energy absorbing composite structure within the context of materials, manufacturing and maintenance for sustainability. *Compos. Struct.* **2021**, *257*, 113081. [[CrossRef](#)]
10. Wang, Y.; Feng, J.; Wu, J.; Hu, D. Effects of fiber orientation and wall thickness on energy absorption characteristics of carbon-reinforced composite tubes under different loading conditions. *Compos. Struct.* **2016**, *153*, 356–368. [[CrossRef](#)]
11. Boria, S.; Scattina, A.; Belingardi, G. Axial energy absorption of CFRP truncated cones. *Compos. Struct.* **2015**, *130*, 18–28. [[CrossRef](#)]
12. Obradovic, J.; Boria, S.; Belingardi, G. Lightweight design and crash analysis of composite frontal impact energy absorbing structures. *Compos. Struct.* **2012**, *94*, 423–430. [[CrossRef](#)]
13. Boria, S.; Scattina, A.; Belingardi, G. Experimental evaluation of a fully recyclable thermoplastic composite. *Compos. Struct.* **2016**, *140*, 21–35. [[CrossRef](#)]
14. Dávila, C.G.; Camanho, P.P.; Turon, A. Effective simulation of delamination in aeronautical structures using shells and cohesive elements. *J. Aircr.* **2008**, *45*, 663–672. [[CrossRef](#)]
15. Sommer, D.E.; Thomson, D.; Falcó, O.; Quino, G.; Cui, H.; Petrinic, N. Damage modelling of carbon fibre composite crush tubes: Numerical simulation and experimental validation of drop weight impact. *Compos. Part Appl. Sci. Manuf.* **2022**, *160*, 107033. [[CrossRef](#)]
16. Garg, R.; Babaei, I.; Paolino, D.S.; Vigna, L.; Cascone, L.; Calzolari, A.; Galizia, G.; Belingardi, G. Predicting composite component behavior using element level crashworthiness tests, finite element analysis and automated parametric identification. *Materials* **2020**, *13*, 4501. [[CrossRef](#)]
17. Wagner, T.; Heimbs, S.; Franke, F.; Burger, U.; Middendorf, P. Experimental and numerical assessment of aerospace grade composites based on high-velocity impact experiments. *Compos. Struct.* **2018**, *204*, 142–152. [[CrossRef](#)]
18. Ma, J.; You, Z. A Novel Origami Crash Box With Varying Profiles. In *ASME Design Engineering Technical Conference*; American Society of Mechanical Engineers: New York, NY, USA, 2014; Volume 6 B. [[CrossRef](#)]
19. ZHAO, X.; HU, Y.; HAGIWARA, I. Shape Optimization to Improve Energy Absorption Ability of Cylindrical Thin-Walled Origami Structure. *J. Comput. Sci. Technol.* **2011**, *5*, 148–162. [[CrossRef](#)]
20. Li, Y.; You, Z. Origami concave tubes for energy absorption. *Int. J. Solids Struct.* **2019**, *169*, 21–40. [[CrossRef](#)]
21. Zhou, C.; Zhou, Y.; Wang, B. Crashworthiness design for trapezoid origami crash boxes. *Thin-Walled Struct.* **2017**, *117*, 257–267. [[CrossRef](#)]
22. Ye, H.; Ma, J.; Zhou, X.; Wang, H.; You, Z. Energy absorption behaviors of pre-folded composite tubes with the full-diamond origami patterns. *Compos. Struct.* **2019**, *221*, 110904. [[CrossRef](#)]
23. Ye, H.; Zhou, X.; Ma, J.; Wang, H.; You, Z. Axial crushing behaviors of composite pre-folded tubes made of KFRP/CFRP hybrid laminates. *Thin-Walled Struct.* **2020**, *149*, 106649. [[CrossRef](#)]

24. Ciampaglia, A.; Fiumarella, D.; Boursier Niutta, C.; Ciardiello, R.; Belingardi, G. Physics based data driven method for the crashworthiness design of origami composite tubes. *Int. J. Mech. Mater. Des.* **2023**, *20*, 445. [[CrossRef](#)]
25. Song, Z.; Ming, S.; Du, K.; Zhou, C.; Wang, Y.; Xu, S.; Wang, B. Energy absorption of metal-composite hybrid tubes with a diamond origami pattern. *Thin-Walled Struct.* **2022**, *180*, 109824. [[CrossRef](#)]
26. O'Neil, J.; Salviato, M.; Yang, J. Energy absorption behavior of filament wound CFRP origami tubes pre-folded in Kresling pattern. *Compos. Struct.* **2023**, *304*, 116376. [[CrossRef](#)]
27. Boreanaz, M.; Belingardi, G.; Maia, C.D.F. Application of the origami shape in the development of automotive crash box. *Mater. Des. Process. Commun.* **2020**, *2*, e181. [[CrossRef](#)]
28. *ASTM D3039-08*; Standard Test Method for Tensile Properties of Polymer Matrix Composite Materials. ASTM International: West Conshohocken, PA, USA, 2008. Available online: <https://www.astm.org/Standards/D3039.htm> (accessed on 10 April 2023).
29. *ASTM D3410-16*; Standard Test Method for Compressive Properties of Polymer Matrix Composite Materials with Unsupported Gage Section by Shear Loading. ASTM International: West Conshohocken, PA, USA, 2016. Available online: <https://www.astm.org/Standards/D3410.htm> (accessed on 10 April 2023).
30. *Formula Student Rules*; Society of Automotive Engineers (SAE): Warrendale, PA, USA, 2023.

Disclaimer/Publisher's Note: The statements, opinions and data contained in all publications are solely those of the individual author(s) and contributor(s) and not of MDPI and/or the editor(s). MDPI and/or the editor(s) disclaim responsibility for any injury to people or property resulting from any ideas, methods, instructions or products referred to in the content.